

Interaction of crystalline topological insulator with an ultrashort laser pulse

Seyyedeh Azar Oliaei Motlagh, Vadym Apalkov, and Mark I. Stockman

Center for Nano-Optics (CeNO) and Department of Physics and Astronomy, Georgia State University, Atlanta, Georgia 30303, USA

(Received 5 January 2017; published 28 February 2017)

We theoretically study the interaction of crystalline topological insulator (CTIs), characterized by surface quadratic gapless bands, with an ultrashort (few-femtosecond) optical pulse. The electron dynamics in such an optical pulse is determined by a strong lattice-momentum dependence of the interband dipole coupling, which is anisotropic and singular at the degeneracy point. The interband mixing induced by the ultrashort pulse results in a finite conduction band population, the distribution of which in the reciprocal space is correlated with the profile of the interband dipole matrix elements and has high contrast. The number of such high-contrast regions depends on the polarization direction of the optical pulse. The ultrashort pulse also causes an electrical current and a net charge transfer through the system in the direction of the maximum field. These findings open up roots to ultrafast optical-field control of the CTIs and petahertz-band optoelectronics.

DOI: [10.1103/PhysRevB.95.085438](https://doi.org/10.1103/PhysRevB.95.085438)**I. INTRODUCTION**

The interaction of ultrashort optical pulses with solids has been the subject of intensive theoretical and experimental research [1–19]. The interest in this field is related to a unique possibility of optical control and optical probing of electron dynamics in solids at a femtosecond time scale, within which the optical pulses have just a few oscillations of the optical field [1–3]. The electric field in such pulses is comparable to the internal fields acting on electrons in solids. Such a strong electric field results in highly nonlinear interband and intraband electron dynamics, strongly modifying both transport and optical properties of solids during the pulse [14,15,20].

An important characteristic of such electron dynamics is its reversibility, i.e., the electron system is highly perturbed during the pulse but returns to its initial state after the pulse. The degree of reversibility (adiabaticity) of the electron dynamics depends on the energy dispersion, especially the band gap, and interband dipole matrix elements, which determine the strength of the interband coupling in the pulse field. It has been shown both experimentally and theoretically [15,16,20], that for dielectrics (fused silica, quartz, and sapphire) the electron dynamics is highly reversible, which is due to large band gaps (~ 10 eV) of such materials and smooth dependence of the interband coupling on the wave vector. The reversibility of electron dynamics in dielectrics can be understood in terms of the dynamics of passage of anticrossing points of Wannier-Stark states belonging to different bands [15,16].

The highly irreversible electron dynamics in ultrashort optical pulses has been predicted theoretically for a two-dimensional (2D) monolayer graphene, which is a semimetal with a gapless energy dispersion relation of relativistic Dirac type in the vicinity of K and K' -points [21–24]. Such irreversibility is characterized by large residual, i.e., after the pulse ends, population of the conduction band (CB). For graphene, the residual CB population is large and comparable to the maximum CB population during the pulse [18]. The origin of the high irreversibility of the electron dynamics in graphene is due to the absence of the band gap and, also, to the unique dependence of the interband dipole coupling on the reciprocal wave vector with a singular behavior of the dipole coupling at the Dirac points, which ultimately results

in the high residual CB population. In addition to the large residual CB population, the electron dynamics in graphene is characterized by high-contrast interference fringes in the distribution of the CB electrons in the reciprocal space. These fringes are caused by the quantum-mechanical interference of the electron passage in the vicinity of the Dirac points, where interband transitions occur due to the singularity of interband dipole couplings [18]. Similar electron behavior in the field of the pulse is expected for three-dimensional (3D) topological insulators, such as $\text{Bi}_x\text{Sb}_{1-x}$, Bi_2Te_3 , Sb_2Te_3 , and Bi_2Se_3 , the surface states of which have gapless relativistic energy dispersion laws similar to graphene [25–32].

Other graphene-like materials, which have 2D honeycomb crystal structures and the corresponding relativistic energy dispersions, are buckled graphene-like materials, such as silicene and germanene [33–41]. The electron dynamics in this case strongly depends on the angle of incidence of the optical pulse and is controlled by the optical field component normal to the plane [19]. At the normal incidence, the electron dynamics is highly irreversible and is similar to that in graphene, while at a large angle of incidence the dynamics becomes partially reversible with a smaller residual CB population. The normal field component of the optical pulse both introduces a finite band gap in the energy dispersion and modifies the interband dipole matrix elements [19].

Here we consider ultrafast electron dynamics in 2D electron systems, which, similar to graphene, are semimetals, but with a quadratic electron-energy dispersion. Such systems are realized at the surface of crystalline topological insulators (CTIs) [42], where the surface states are protected by the time-reversal and discrete rotational symmetries. An example of such a CTI is a tetragonal crystal with the C_4 symmetry, where the quadratic gapless bands are predicted to occur at the (001) crystal face [42]. Below we study the electron dynamics in such materials under ultrashort optical pulses assuming that the dynamics is coherent and considering low-energy effective models for the surface state of CTI. The assumption that the dynamics is coherent is valid as long as the duration of the pulse, which is ≈ 4 fs, is less than the characteristic electron scattering time in these materials, which one would expect on a time scale longer than 10 fs as in graphene (see the following paragraph).

Experimentally, the processes of energy-momentum relaxation in the photoexcited CB electron population occur during times ranging from ~ 10 -20 fs to ~ 200 -800 fs [43–50]. The shortest ~ 10 fs, times are due to ultrafast electron-electron interactions, while longer, ~ 1 ps, times are those of phonon-assisted cooling.

We predict below that the ultrafast interband electron dynamics in CTIs results in characteristic CB electron distribution, which is formed due to the quantum-mechanical interference of the excitation events during consecutive crossing of lines in the reciprocal space of $\mathbf{k}_x = \epsilon \mathbf{k}_y$ (where $|\epsilon| \leq 1$ is a constant) near the degeneracy point (Γ point) in the reciprocal space. At these lines, the dipole transitions are strongly enhanced. A fundamental difference from graphene is a high degree of anisotropy of the low-energy dispersion, which results in a strong dependence on the polarization plane of the optical pulse. In particular, the CB population distribution in the reciprocal space has a single-peak or double-peak structure for different polarizations of the optical pulse.

II. MODEL AND MAIN EQUATIONS

We describe surface states of a CTI within an effective low-energy model determined by the following Hamiltonian [42]:

$$\mathcal{H}_0 = \frac{\hbar^2 k^2}{2m_0} + \frac{\hbar^2(k_x^2 - k_y^2)}{2m_1} \sigma_z + \frac{\hbar^2 k_x k_y}{2m_2} \sigma_x, \quad (1)$$

where σ_x, σ_z are Pauli matrices, m_0, m_1, m_2 are effective masses, and (k_x, k_y) is a 2D wave vector with magnitude k . The Hamiltonian, \mathcal{H}_0 , describes the valence band (VB) and the CB with the following energy dispersion:

$$E_{c,v} = \frac{\hbar^2 k^2}{2m_0} \pm \hbar^2 \sqrt{\left(\frac{k_x^2 - k_y^2}{2m_1}\right)^2 + \left(\frac{k_x k_y}{2m_2}\right)^2} \quad (2)$$

with corresponding two-component wave functions $\Psi_{\mathbf{k}}^{(\alpha)}(\mathbf{r})$, where $\alpha = v$ (valence band) and c (conduction band). The energy dispersion has quadratic band degeneracy at $k = 0$ which is anisotropic.

Within the effective Hamiltonian (1), we consider the interaction of an electron system at the surface of a CTI with an ultrashort optical pulse, which is parametrized by the following form:

$$F(t) = F_0 e^{-u^2} (1 - 2u^2), \quad (3)$$

where F_0 is the amplitude of the pulse, $u = t/\tau$, and τ is the pulse length, which is set as $\tau = 1$ fs. We assume that the pulse is linearly polarized, where the plane of polarization is characterized by angle θ measured relative to axis x .

The time-dependent Hamiltonian of an electron in the field of the pulse takes the following form:

$$\mathcal{H}(t) = \mathcal{H}_0 - e\mathbf{F}(t)\mathbf{r}, \quad (4)$$

where $\mathbf{F}(t) = F(t)(\cos \theta, \sin \theta)$, and e is electron charge. Electron dynamics is described by the time-dependent Schrödinger equation,

$$i\hbar \frac{d\Psi}{dt} = \mathcal{H}\Psi. \quad (5)$$

Intraband (within a single band) electron dynamics is determined by the Bloch acceleration theorem [51], which describes the electron intraband dynamics for both conduction and valence bands,

$$\hbar \frac{d\mathbf{k}}{dt} = e\mathbf{F}(t). \quad (6)$$

For an electron with initial wave vector (lattice momentum) \mathbf{q} , the intraband electron dynamics is described by the time-dependent wave vector, $\mathbf{k}(\mathbf{q}, t)$, which is given by the solution of Eq. (6),

$$\mathbf{k}(\mathbf{q}, t) = \mathbf{q} + \frac{e}{\hbar} \mathbf{A}(t), \quad \mathbf{A}(t) = \int_{-\infty}^t \mathbf{F}(t_1) dt_1, \quad (7)$$

where \mathbf{A} is often called ‘‘vector potential’’ since it is a vector potential in a specific gauge. The corresponding wave functions, which are solutions of Schrödinger equation (5) within a single band approximation, i.e., without interband coupling, are the Houston functions [52],

$$\Phi_{\alpha\mathbf{q}}^{(H)}(\mathbf{r}, t) = \Psi_{\mathbf{k}(\mathbf{q}, t)}^{(\alpha)}(\mathbf{r}) e^{-i/\hbar \int_{-\infty}^t dt_1 E_{\alpha}[\mathbf{k}(\mathbf{q}, t_1)]}, \quad (8)$$

where $\alpha = v$ or c for the VB and the CB, respectively.

We express the general solution of the Schrödinger equation (5) in the basis of Houston functions:

$$\Psi_{\mathbf{q}}(\mathbf{r}, t) = \sum_{\alpha=v,c} \beta_{\alpha\mathbf{q}}(t) \Phi_{\alpha\mathbf{q}}^{(H)}(\mathbf{r}, t), \quad (9)$$

where $\beta_{\alpha\mathbf{q}}(t)$ are expansion coefficients, which satisfy the following system of equations:

$$\frac{d\beta_{c\mathbf{q}}(t)}{dt} = -i \frac{\mathbf{F}(t)\mathbf{Q}_{\mathbf{q}}(t)}{\hbar} \beta_{v\mathbf{q}}(t), \quad (10)$$

$$\frac{d\beta_{v\mathbf{q}}(t)}{dt} = -i \frac{\mathbf{F}(t)\mathbf{Q}_{\mathbf{q}}^*(t)}{\hbar} \beta_{c\mathbf{q}}(t), \quad (11)$$

where vector functions $\mathbf{Q}_{\mathbf{q}}(t)$ are related to the interband dipole matrix elements, \mathbf{D} ,

$$\mathbf{Q}_{\mathbf{q}}(t) = \mathbf{D}[\mathbf{k}(\mathbf{q}, t)] e^{-i/\hbar \int_{-\infty}^t dt_1 [E_c[\mathbf{k}(\mathbf{q}, t_1)] - E_v[\mathbf{k}(\mathbf{q}, t_1)]]}, \quad (12)$$

$$\mathbf{D}(\mathbf{k}) = \langle \Psi_{\mathbf{k}}^{(c)} | e\mathbf{r} | \Psi_{\mathbf{k}}^{(v)} \rangle. \quad (13)$$

With the known wave functions of the conduction and valence bands calculated from Hamiltonian (1), we obtain the following expressions for the x and y components of the dipole matrix elements:

$$D_x(\mathbf{k}) = \frac{e}{2i} \mu \frac{k_y(k_x^2 + k_y^2)}{(k_x^2 - k_y^2)^2 + k_x^2 k_y^2 \mu^2} \quad (14)$$

and

$$D_y(\mathbf{k}) = \frac{-e}{2i} \mu \frac{k_x(k_x^2 + k_y^2)}{(k_x^2 - k_y^2)^2 + k_x^2 k_y^2 \mu^2}, \quad (15)$$

where $\mu = m_1/m_2$. The dipole matrix elements, D_x and D_y , have maxima at the degeneracy point, $k = 0$. Near this point, the properties of the interband dipole coupling depend on polarization of the optical pulse, i.e., on angle θ , and on the ratio of effective masses, μ . For a given linear polarization of

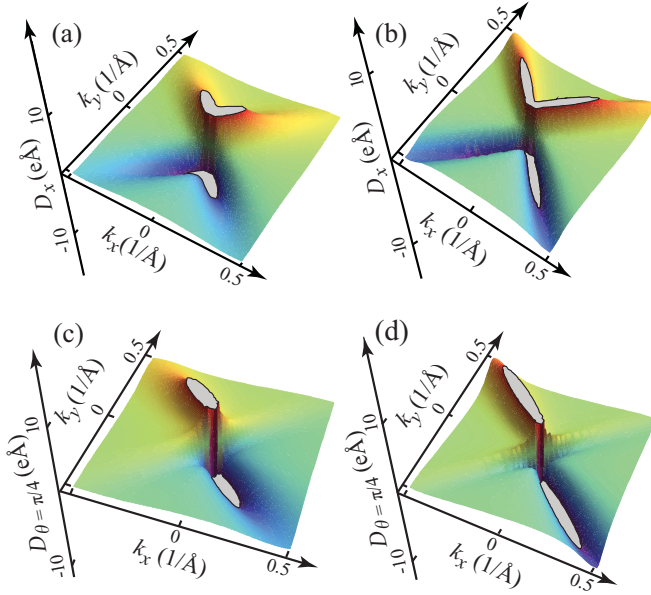


FIG. 1. Interband dipole matrix element D_θ . (a) Polarization of the pulse is along axis x ($\theta = 0$) and $\mu = 1$. (b) The same as (a) but for $\mu = 0.5$. (c) Polarization of the pulse is along the diagonal ($\theta = \pi/4$) and $\mu = 1$. (d) The same as (c) but for $\mu = 0.5$.

the pulse, the effective interband coupling is determined by the following expression:

$$D_\theta(\mathbf{k}) = D_x(\mathbf{k}) \cos \theta + D_y(\mathbf{k}) \sin \theta. \quad (16)$$

The intraband dynamics determines the electron trajectory in the reciprocal space, which is along the direction of polarization of the pulse as given by Eq. (7). Along this trajectory, the interband coupling is characterized by effective dipole matrix element $D_\theta(\mathbf{k})$ as a function of crystal momentum k has either one or two peaks, as illustrated in Fig. 1. This is in contrast to a graphene monolayer, for which the effective coupling always has only one peak.

For the pulse polarization along the axis of symmetry of the system, i.e., axis x or y , the dipole coupling has two peaks [cf. Figs. 1(a) and 1(b)]. For example, for $\theta = 0$ (polarization along axis x), the effective coupling is $D_{\theta=0} = D_x$ [see Eq. (14)]. In the reciprocal space, dipole matrix element D_x has two maxima as shown in Figs. 1(a) and 1(b). These maxima are at

$$\frac{k_x}{k_y} = \pm \sqrt{\sqrt{4 - \mu^2} - 1}. \quad (17)$$

With decreasing μ , the corresponding peaks become narrower as shown in Fig. 1(b), while the area under each peak does not depend on μ , i.e., $\int_{-\infty}^0 D_x dk_x = \int_0^{\infty} D_x dk_x = e\pi/2i$. For a generic direction of polarization, i.e., $\theta \neq \pi/4$, the effective dipole matrix element, D_θ , always has two peaks in the reciprocal space similar to Figs. 1(a) and 1(b). Only for $\theta = \pi/4$, this behavior degenerates to having only one peak as shown in Figs. 1(c) and 1(d).

We solve numerically the system of equations (10) and (11) with initial condition $\beta_{v\mathbf{q}} = 1$, which corresponds to the initial population in the VB. We characterize the corresponding electron dynamics in terms of the CB population, generated electric

current, and the transferred charge. The time-dependent CB population is defined as $N_{CB}(\mathbf{q}, t) = |\beta_{c\mathbf{q}}(t)|^2$, where the residual value of the CB population, $N_{CB}^{(res)}(\mathbf{q})$, is defined as the population after the pulse. We study below both $N_{CB}^{(res)}(\mathbf{q})$ as a function of lattice momentum and the net residual CB population,

$$N^{(res)} = \sum_{\mathbf{q}} N_{CB}^{(res)}(\mathbf{q}). \quad (18)$$

The electric current, $\mathbf{J}(t) = [J_x(t), J_y(t)]$, generated during the pulse is determined by the following expression:

$$J_j(t) = \frac{e}{a^2} \sum_{\mathbf{q}} \sum_{\alpha_1, \alpha_2=v,c} \beta_{\alpha_1\mathbf{q}}^* V_j^{\alpha_1\alpha_2} \beta_{\alpha_2\mathbf{q}}(t), \quad (19)$$

where $j = x, y$ and $V_j^{\alpha_1\alpha_2}$ are the matrix elements of the velocity operator

$$\hat{V}_j = \frac{1}{\hbar} \frac{\partial H_0}{\partial k_j}, \quad (20)$$

calculated between the CB and VB states. These matrix elements have the following forms:

$$V_x^{cv} = i D_x(\mathbf{k}) [E_c(\mathbf{k}) - E_v(\mathbf{k})] / \hbar, \quad (21)$$

$$V_y^{cv} = i D_y(\mathbf{k}) [E_c(\mathbf{k}) - E_v(\mathbf{k})] / \hbar, \quad (22)$$

$$V_x^{cc} = \hbar k_x \left(\frac{1}{m_0} + \frac{1}{m_1} \frac{(k_x^2 - k_y^2) + \frac{1}{2}\mu^2 k_y^2}{\sqrt{(k_x^2 - k_y^2)^2 + \mu^2(k_x k_y)^2}} \right), \quad (23)$$

$$V_y^{cc} = \hbar k_y \left(\frac{1}{m_0} + \frac{1}{m_1} \frac{(k_y^2 - k_x^2) + \frac{1}{2}\mu^2 k_x^2}{\sqrt{(k_x^2 - k_y^2)^2 + \mu^2(k_x k_y)^2}} \right), \quad (24)$$

$$V_x^{vv} = \hbar k_x \left(\frac{1}{m_0} - \frac{1}{m_1} \frac{(k_x^2 - k_y^2) + \frac{1}{2}\mu^2 k_y^2}{\sqrt{(k_x^2 - k_y^2)^2 + \mu^2(k_x k_y)^2}} \right), \quad (25)$$

$$V_y^{vv} = \hbar k_y \left(\frac{1}{m_0} - \frac{1}{m_1} \frac{(k_y^2 - k_x^2) + \frac{1}{2}\mu^2 k_x^2}{\sqrt{(k_x^2 - k_y^2)^2 + \mu^2(k_x k_y)^2}} \right). \quad (26)$$

With the current given by Eq. (19), we can calculate the charge transferred during the pulse,

$$Q_{tr,j} = \int_{-\infty}^{\infty} dt J_j(t). \quad (27)$$

III. RESULTS AND DISCUSSION

The results presented in this section have been obtained for the following parameters of the system: $m_0 = m_e$, $m_2 = m_e$, and different values of parameter $\mu = m_1/m_2$, where m_e is electron mass.

In Fig. 2 the residual conduction band population, $N_{CB}^{(res)}(\mathbf{k})$, is shown as a function of wave vector \mathbf{k} for different polarizations, i.e., angle θ , of the optical pulse and different values of parameter μ . The distribution of $N_{CB}^{(res)}(\mathbf{k})$ shows high-contrast peaks, localized near the local maximum of the effective interband dipole coupling (cf. Fig. 1). Note the fourfold rotational symmetry of distribution $N_{CB}^{(res)}$ in Fig. 2.

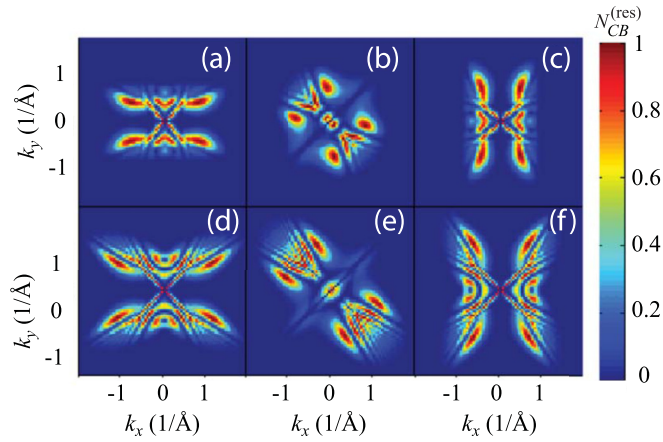


FIG. 2. Residual conduction band population $N_{CB}^{(res)}$ as a function of wave vector \mathbf{k} for different values of parameter μ and angle θ . The amplitude of the pulse is $F_0 = 1$ V/Å. (a) $\mu = 1$, $\theta = 0$; (b) $\mu = 1$, $\theta = \pi/4$; (c) $\mu = 1$, $\theta = \pi/2$; (d) $\mu = 0.5$, $\theta = 0$; (e) $\mu = 0.5$, $\theta = \pi/4$; (f) $\mu = 0.5$, $\theta = \pi/2$.

In Fig. 2, a region of large $N_{CB}^{(res)}$ contains fringes of high and low residual CB population. These fringes are due to the interference of two passages per optical period of the same region of enhanced interband coupling (see Appendix for more discussion). This fringe structure is more developed with larger number of fringes for smaller values of μ [see Figs. 2(d)–2(f)]. This is due to the fact that D_x becomes more localized and extended to larger values of k_y for smaller values of μ [see Fig. 1(a)]. Generally, this fringe structure is a self-referenced interferogram that contains information about dispersion and topological curvature of the electronic bands.

The net residual CB population, $N^{(res)}$, is shown in Fig. 3 as a function of the pulse amplitude, F_0 . The dependence of $N^{(res)}$ on angle θ is different for smaller, $\mu = 0.5$, and larger, $\mu = 1.0$, values of μ . For $\mu = 0.5$, the net CB population is almost isotropic for all amplitudes of the pulse with small anisotropy at $F_0 < 1$ V/Å [see Fig. 3(b)]. For $\mu = 1.0$, the net CB population is isotropic for small field amplitudes, but becomes highly anisotropic at large amplitudes, $F_0 > 1.0$ V/Å [see Fig. 3(a)]. At such large amplitudes, the residual CB population is the smallest at $\theta = 0$. Similar anisotropy is also expected for $\mu = 1.0$, but for larger pulse amplitude, $F_0 > 2$ V/Å. The origin of such anisotropy is the overlap of two regions of large $N_{CB}^{(res)}(\mathbf{k})$ for polarization angle $\theta = 0$. These regions correspond to two maxima of interband dipole coupling, D_x . Since these maxima are more localized for smaller values of μ , then the anisotropy in $N^{(res)}(\theta)$ is more pronounced at $\mu = 0.5$.

The finite CB population during the pulse also produces an electric current, $\mathbf{J}(t)$, which can be found from Eq. (19). In Fig. 4, the current density, $\mathbf{J}(t)$, is shown as a function of time together with the corresponding vector potential, which is the time integral of the electric field. The current density almost follows the profile of the vector potential. The generated electric current results in finite charge transfer, Q_{tr} , which is defined by Eq. (27). From the current dynamics, shown in

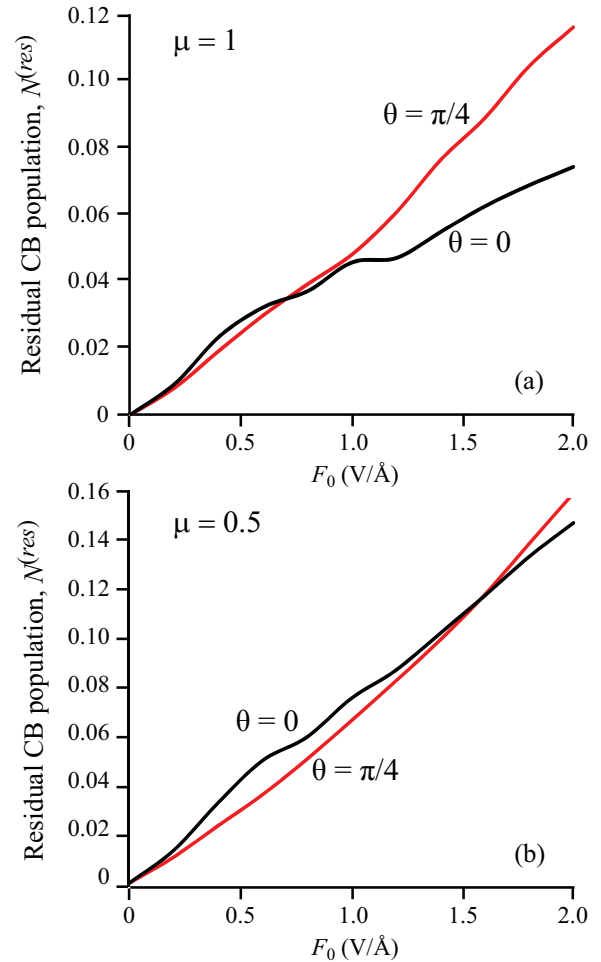


FIG. 3. Residual conduction band population as a function of pulse amplitude F_0 for different values of angle θ (polarization of the pulse) and parameter μ . The black lines correspond to $\alpha = 0$ (polarization along axis x) and the dashed lines show the results for $\theta = \pi/4$. The values of parameter μ are 1.0 (a) and 0.5 (b).

Fig. 4, it follows that the transferred charge is positive, which means that the direction of the charge transfer is the same as the direction of the field maximum.

The calculated transferred charge is shown in Fig. 5 as a function of the field amplitude, F_0 . The transferred charge is positive for all F_0 . It is approximately inversely proportional to parameter μ (see Fig. 5). There is also a weak dependence

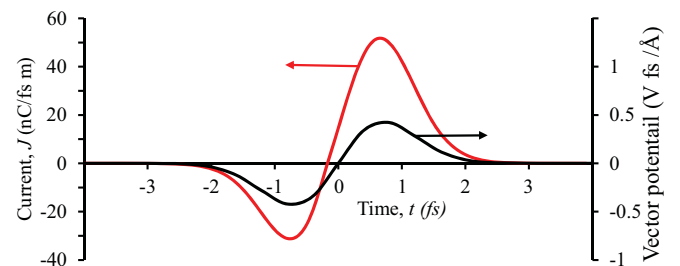


FIG. 4. Electric current density as a function of time for amplitude $F_0 = 1.0$ V/Å. The parameter μ is 1.0. The red line shows the corresponding vector potential, $\mathbf{A}(t)$.

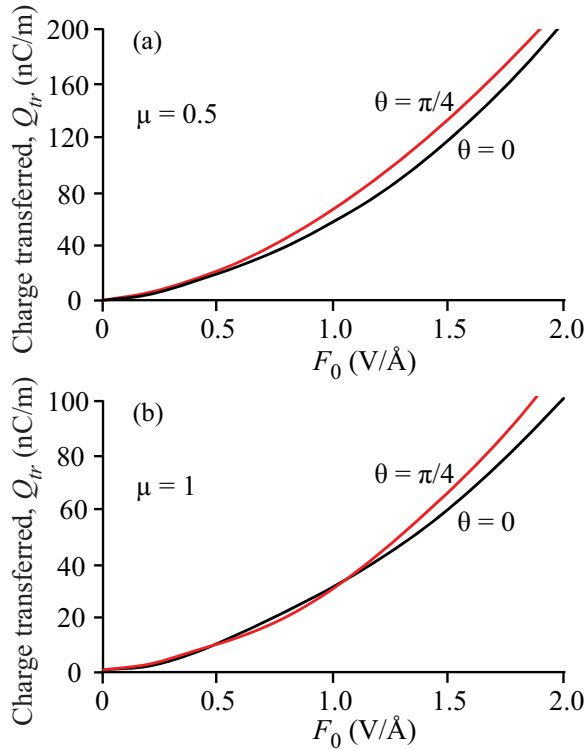


FIG. 5. Transferred charge density through the system as a function of F_0 for different values of parameter μ and angle θ (polarization of the pulse).

of Q_{tr} on the pulse polarization, i.e., angle θ . While for the net residual CB population, there is a strong dependence of $N^{(res)}$ on angle θ , e.g., at $\mu = 1$ and $F_0 = 2.0 \text{ V/\AA}$, $N^{(res)}$ changes by almost 50% with θ , the transferred charge is almost isotropic with angle variations less than 5%.

For $\mu = 0.5$, the transferred charge, Q_{tr} , has the largest value at polarization angle $\theta = \pi/4$ for all amplitudes of the pulse. For $\mu = 1.0$, the transferred charge as a function of angle θ has maximum value at $\theta = 0$ for small amplitudes, $F_0 \lesssim 1 \text{ V/\AA}$, while at large amplitudes, $F_0 > 1 \text{ V/\AA}$, the maximum of Q_{tr} is realized at $\theta = \pi/4$. Thus, if Q_{tr} is measured as a function of angle θ at a given amplitude of the pulse, then for different amplitudes F_0 we expect different behavior. While for all F_0 the transferred charge as a function of θ has the periodicity of $\pi/2$, the positions of maxima and minima depend on F_0 and μ . If the system is characterized by parameter $\mu = 0.5$, then for all amplitudes F_0 , the maximum of Q_{tr} occurs at $\theta = \pi/4$ and the minimum is at $\theta = 0$ or $\pi/2$. For larger values of μ , e.g., $\mu = 1.0$, at small amplitude F_0 , the maximum of Q_{tr} is at $\theta = 0$ (or $\pi/2$) and the minimum is at $\theta = \pi/8$ [see Fig. 6(b)]. At larger amplitude F_0 , the maximum of Q_{tr} is at $\theta = \pi/8$ and the minimum is at $\theta = 0$ ($\pi/2$) [see Fig. 6(a)].

IV. CONCLUSION

Interband electron dynamics in an ultrashort optical pulse field strongly depends on the distribution of the interband dipole matrix elements in the reciprocal space. For the surface states of a topological crystalline insulator with quadratic gapless bands, the interband dipole matrix elements are

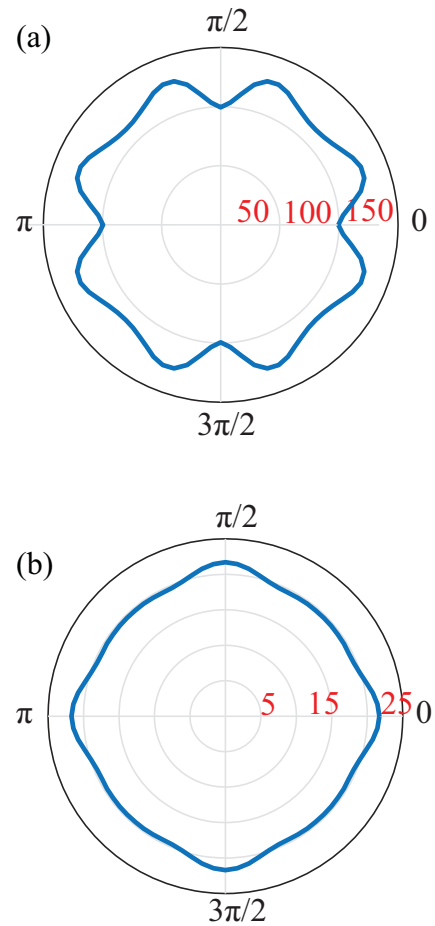


FIG. 6. Transferred charge density through the system as a function of angle θ for $\mu = 1.0$. The transferred charge is calculated along the direction of polarization of the pulse. The amplitude of the optical pulse is (a) $F_0 = 2.0 \text{ V/\AA}$ and (b) $F_0 = 0.8 \text{ V/\AA}$.

singular at the degeneracy point and are anisotropic around this point. The distribution of the residual CB population in the reciprocal space is correlated with the corresponding distribution of the interband dipole matrix elements. Namely, the distribution of CB population, $N_{CB}^{(res)}$, shows high-contrast peaks, localized near the local maximum of the interband dipole coupling. The number of the high-contrast peaks in $N_{CB}^{(res)}$ is correlated with the number of peaks in the dipole matrix elements as a function of wave vector along the direction of pulse polarization. The number of peaks changes from four to two with rotation of the polarization direction.

The ultrashort optical pulse causes the charge transfer through the system. The charge is transferred in the direction of the maximum field. The magnitude of the transferred charge depends on the amplitude of the pulse and the direction of the pulse polarization.

ACKNOWLEDGMENTS

Major funding was provided by Grant No. DE-FG02-01ER15213 from the Chemical Sciences, Biosciences and Geosciences Division, Office of Basic Energy Sciences, Office of Science, US Department of Energy. Numerical simulations

have been performed using support by Grant No. DE-FG02-11ER46789 from the Materials Sciences and Engineering Division of the Office of the Basic Energy Sciences, Office of Science, U.S. Department of Energy. The work of V.A. was supported by Grant No. ECCS-1308473 from NSF.

APPENDIX

To illustrate the nonmonotonic dependence of the residual conduction band population in the reciprocal space along the line of maxima of the interband dipole matrix element, we consider a simplified model of the interband coupling. For concreteness we assume that the pulse is polarized along axis x ($\theta = 0$). In this case the interband dipole matrix element as a function of k_x has two maxima. We consider the electron dynamics near one these maxima.

For the x -polarized optical pulse the electron trajectory is determined by an acceleration theorem and is shown schematically in Fig. 7(a) for initial wave vector $(k_{x,0}, k_{y,0})$. Such trajectory passes twice though the maximum of the dipole matrix elements, which is shown by a dashed line. Such passages occur at moments of time t_1 and t_2 . These moments of time correspond to equal values of vector potential as shown in Fig. 7(b). At these points the electric field has different values, F_1 and F_2 [see Fig. 7(c)].

To describe the interband dynamics corresponding to the trajectory shown in Fig. 7(a) we approximate the interband dipole coupling by a steplike function, which is nonzero and constant only within narrow interval $k_{x,max} - \delta_x/2 < k_x < k_{x,max} + \delta_x/2$, where $k_{x,max}$ is the position of the maximum of D_x and δ_x is the width of the maximum (see Fig. 8). The value of the dipole matrix element within this interval is $i\Delta_0/e$, where Δ_0 is related to Δ_x as $\Delta_0\delta_x = \pi/2$. The value of the dipole matrix element at the peak and, correspondingly, the width of the peak depend on $k_{y,0}$. With increasing $k_{y,0}$, maximum D_0 decreases and width Δ_0 increases.

We also assume that the width δ_x is small so that within the region of nonzero constant dipole matrix element, the energies, E_c and E_v , of the VB and CB levels and the electric field, F_c , are constant. Under these assumptions, the interband mixing occurs only within the region $k_{x,max} - \delta_x/2 < k_x < k_{x,max} + \delta_x/2$, where the system of equations (10) and (11) takes the form

$$\frac{d\beta_{c\mathbf{q}}(t)}{dt} = -\frac{i}{\hbar}\Delta_0 F_c e^{-i(E_c - E_v)t/\hbar} \beta_{v\mathbf{q}}(t), \quad (\text{A1})$$

$$\frac{d\beta_{v\mathbf{q}}(t)}{dt} = -\frac{i}{\hbar}\Delta_0 F_c e^{-i(E_c - E_v)t/\hbar} \beta_{c\mathbf{q}}(t). \quad (\text{A2})$$

Taking into account acceleration theorem (6), we change the variable from t to k_x in the system of equations (A1) and (A2). The new system of equations becomes

$$\frac{d\beta_{c\mathbf{q}}(k_x)}{dk_x} = -i\Delta_0 e^{-i\kappa k_x} \beta_{v\mathbf{q}}(k_x), \quad (\text{A3})$$

$$\frac{d\beta_{v\mathbf{q}}(k_x)}{dk_x} = -i\Delta_0 e^{i\kappa k_x} \beta_{c\mathbf{q}}(k_x), \quad (\text{A4})$$

where $\kappa = (E_c - E_v)/eF_c$. Solution of the system of equations (A3) and (A4) determines the relation between the coeffi-

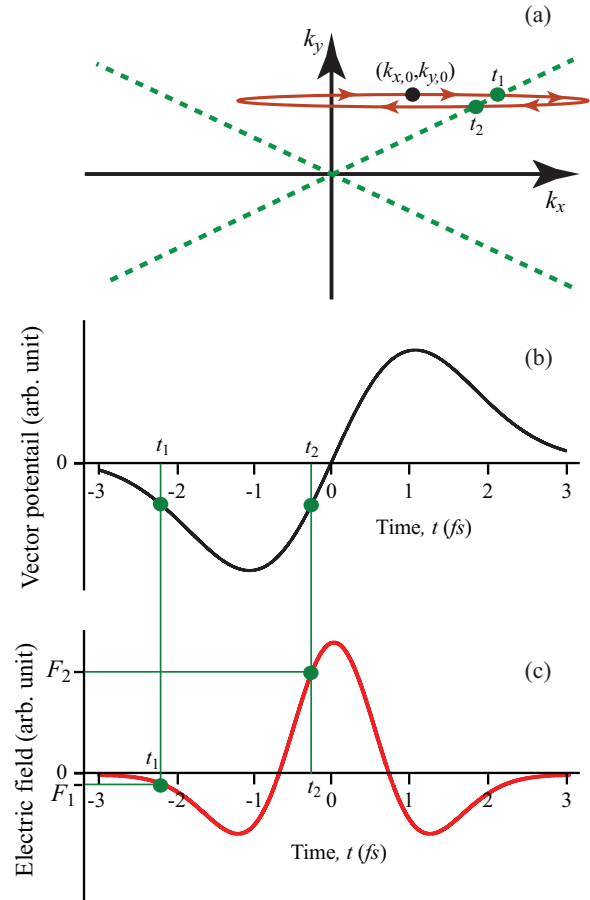


FIG. 7. Illustration of electron interband dynamics for the x -polarized optical pulse. (a) Dashed lines show the positions of the maxima of the interband dipole coupling. The red line illustrates the electron trajectory in the reciprocal space, where $(k_{x,0}, k_{y,0})$ is the initial electron wave vector. The electron trajectory passes twice the region of large interband coupling (dashed line) at two moments of time, t_1 and t_2 . These passages are shown by green dots (for x -polarized pulse these points coincide, but for illustration purposes the dots are shifted in space). (b) Vector potential of the optical pulse as a function of time. The moments of time t_1 and t_2 are the same as in panel (a). At these moments the vector potential is the same. (c) The electric field of the optical pulse as a function of time. At the moments of time t_1 and t_2 the magnitudes of electric field are not the same, $F_2 > F_1$.

icients $\hat{\beta}_L = (\beta_{c,L}, \beta_{v,L})$ at $k_x = k_{x,max} - \delta_x/2$ and coefficients $\hat{\beta}_R = (\beta_{c,R}, \beta_{v,R})$ at $k_x = k_{x,max} + \delta_x/2$,

$$\hat{\beta}_R = \hat{T}(\kappa)\hat{\beta}_L, \quad (\text{A5})$$

where $\hat{T}(\kappa)$ is the transfer matrix, which is given by the following expression:

$$\hat{T}(\kappa) = i\hat{R}_\phi \hat{\Xi}_{\gamma,\Lambda}, \quad (\text{A6})$$

$$\hat{R}_\phi = \begin{pmatrix} e^{-i\phi} & 0 \\ 0 & e^{-i\phi} \end{pmatrix}, \quad (\text{A7})$$

$$\hat{\Xi}_{\gamma,\Lambda} = \begin{pmatrix} -\cos \gamma e^{-\Lambda} & \sin \gamma \\ \sin \gamma & \cos \gamma e^{\Lambda} \end{pmatrix}. \quad (\text{A8})$$

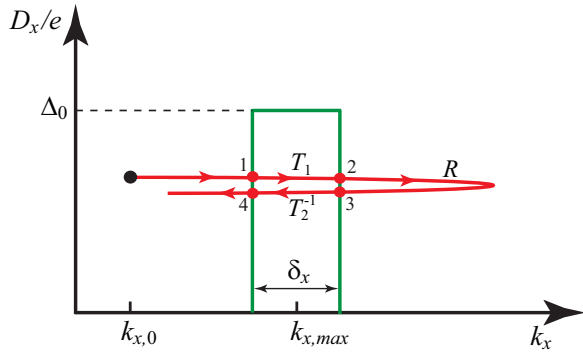


FIG. 8. Approximation for the interband dipole coupling near the maximum. The width of the peak is δ_x and its height Δ_0 . Red line illustrates part of the electron trajectory in the reciprocal space—see Fig. 7(a). The trajectory passes twice through the maximum of the interband coupling. Along the trajectory strong interband mixing occurs only between points “1” and “2”, and “3” and “4”. The values of $\hat{\beta}$ at points “2” and “1” are related by transfer matrix T_1 , at points “2” and “3” - by accumulation of dynamic phase, which is described by rotational matrix R , and at points “3” and “4” - by transfer matrix T_2 .

Here the angles ϕ , γ , and Λ are defined by the following expressions:

$$\phi = \kappa \delta_x, \quad (\text{A9})$$

$$\gamma = -\arcsin \left[\frac{\sin \left(\frac{\pi}{2} \sqrt{1 + (\kappa/2\Delta_0)^2} \right)}{\sqrt{1 + (\kappa/2\Delta_0)^2}} \right], \quad (\text{A10})$$

and

$$\Lambda = \arctan \left[\sqrt{1 + \left(\frac{2\Delta_0}{\kappa} \right)^2} \cot \left(\frac{\pi}{2} \sqrt{1 + \left(\frac{\kappa}{2\Delta_0} \right)^2} \right) \right]. \quad (\text{A11})$$

Then the electron interband dynamics along the trajectory shown in Fig. 8 by the red line is described by the following set of expressions: (i) between points “1” and “2” (see Fig. 8) the expansion coefficients $\hat{\beta}_2$ and $\hat{\beta}_1$ are related by the transfer matrix $\hat{T}(\kappa_1)$,

$$\hat{\beta}_2 = \hat{T}(\kappa_1)\hat{\beta}_1, \quad (\text{A12})$$

where $\kappa_1 = (E_c - E_v)/eF_1$. (ii) Between points “2” and “3” the interband dipole matrix element is zero, then the electron dynamics between these points is determined by accumulation of the dynamics phases without any interband mixing,

$$\hat{\beta}_3 = \hat{R}_\xi \hat{\beta}_2, \quad (\text{A13})$$

where angle $\xi = \int_{t_1}^{t_2} E_c(t)dt/\hbar$ depends on the path length between points “2” and “3”. (iii) between points “3” and “4” the expansion coefficients $\hat{\beta}_3$ and $\hat{\beta}_4$ are related by the transfer matrix $\hat{T}(\kappa_2)$,

$$\hat{\beta}_4 = \hat{T}^{-1}(\kappa_2)\hat{\beta}_3, \quad (\text{A14})$$

where $\kappa_2 = (E_c - E_v)/eF_2$.

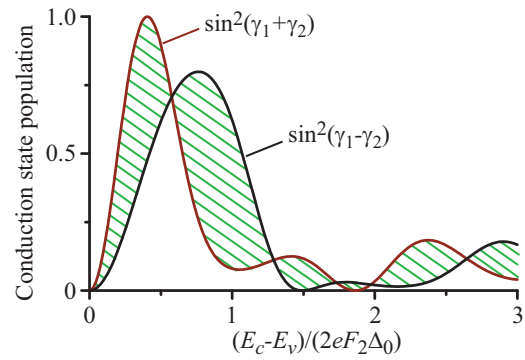


FIG. 9. Residual population, $|\beta_c|^2$, of the conduction band state with initial wave vector $(k_{x,0}, k_{y,0})$ as a function of $\kappa_2/2\Delta_0 = (E_c - E_v)/(2eF_2\Delta_0)$. The parameter, κ_1 , is $3\kappa_2$. The red line shows the function $\sin^2(\gamma_1 + \gamma_2)$, while the black line corresponds to $\sin^2(\gamma_1 - \gamma_2)$. Possible values of residual conduction band population are shown by dashed regions.

Combining relations (A12)–(A14), we obtain

$$\hat{\beta}_4 = \hat{T}^{-1}(\kappa_2)\hat{R}_\xi \hat{T}(\kappa_1)\hat{\beta}_1. \quad (\text{A15})$$

Substituting Eq. (A6) into expression (A15), we derive

$$\hat{\beta}_4 = \hat{\Xi}_{\gamma_2, -\Lambda_2} \hat{R}_{\xi + \phi_1 - \phi_2} \hat{\Xi}_{\gamma_1, \Lambda_1} \hat{\beta}_1, \quad (\text{A16})$$

where the indexes 1 and 2 correspond to two values of electric field F_1 and F_2 , respectively. Since $\beta_1 = (0, 1)$ (in the initial state the valence band is occupied), the residual conduction band population, which is the conduction band component of $\hat{\beta}_4$, is

$$|\beta_c|^2 = \cos^2 \gamma_2 \sin^2 \gamma_1 + \cos^2 \gamma_1 \sin^2 \gamma_2 - \frac{1}{2} \sin(2\gamma_1) \sin(2\gamma_2) \cos \varphi, \quad (\text{A17})$$

where $\varphi = \Lambda_2 - \Lambda_1 + 2(\xi + \phi_1 - \phi_2)$, which depends on electron initial wave vectors. The magnitude of the residual conduction band population is in the range

$$\min\{\sin^2(\gamma_1 - \gamma_2), \sin^2(\gamma_1 + \gamma_2)\} < |\beta_c|^2 < \max\{\sin^2(\gamma_1 - \gamma_2), \sin^2(\gamma_1 + \gamma_2)\}. \quad (\text{A18})$$

The difference between γ_1 and γ_2 is in the value of electric field; all other parameters ($E_c - E_v$, Δ_0) are the same. The corresponding electric fields are shown in Fig. 7, where $F_2 > F_1$. In Fig. 9 we show $\sin^2(\gamma_1 - \gamma_2)$ and $\sin^2(\gamma_1 + \gamma_2)$ as a function of parameter $\kappa_2/2\Delta_0$ assuming that $\kappa_1 = 3\kappa_2$, i.e., $F_2 = 3F_1$. The possible values of $|\beta_c|^2$ are within the dashed region. Since the magnitude of Δ_0 is correlated with the position of the point along the dashed line of maxima [see Fig. 7(a)], i.e., with increasing k_y along the line of maxima, interband coupling Δ_0 decreases (at $k_y = 0$, $D_0 \rightarrow \infty$ and at $k_y \rightarrow \infty$, $D_0 = 0$), then the results shown in Fig. 9 illustrate the fact the maximum of $|\beta_c|^2$ is at a finite distance from the degeneracy point, $k = 0$.

- [1] M. Gertszvolf, M. Spanner, D. M. Rayner, and P. B. Corkum, *J. Phys. B* **43**, 131002 (2010).
- [2] A. V. Mitrofanov, A. J. Verhoef, E. E. Serebryannikov, J. Lumeau, L. Glebov, A. M. Zheltikov, and A. Baltuška, *Phys. Rev. Lett.* **106**, 147401 (2011).
- [3] M. Lenzen, J. Kruger, S. Sartania, Z. Cheng, C. Spielmann, G. Mourou, W. Kautek, and F. Krausz, *Phys. Rev. Lett.* **80**, 4076 (1998).
- [4] R. H. Fowler and L. Nordheim, *Proc. R. Soc. London, Ser. A* **119**, 173 (1928).
- [5] C. Zener, *Proc. R. Soc. A* **145**, 523 (1934).
- [6] L. V. Keldysh, *J. Exp. Theor. Phys.* **33**, 994 (1957) [*Sov. Phys. JETP* **6**, 763 (1958)].
- [7] G. H. Wannier, *Phys. Rev.* **117**, 432 (1960).
- [8] M. Lenzlinger and E. H. Snow, *J. Appl. Phys.* **40**, 278 (1969).
- [9] M. Kruger, M. Schenk, and P. Hommelhoff, *Nature (London)* **475**, 78 (2011).
- [10] S. Ghimire, A. D. DiChiara, E. Sistrunk, P. Agostini, L. F. DiMauro, and D. A. Reis, *Nat. Phys.* **7**, 138 (2011).
- [11] M. Durach, A. Rusina, M. F. Kling, and M. I. Stockman, *Phys. Rev. Lett.* **105**, 086803 (2010).
- [12] L. Miaja-Avila, C. Lei, M. Aeschlimann, J. L. Gland, M. M. Murnane, H. C. Kapteyn, and G. Saathoff, *Phys. Rev. Lett.* **97**, 113604 (2006).
- [13] M. Durach, A. Rusina, M. F. Kling, and M. I. Stockman, *Phys. Rev. Lett.* **107**, 086602 (2011).
- [14] A. Schiffrin, T. Paasch-Colberg, N. Karpowicz, V. Apalkov, D. Gerster, S. Muhlbrandt, M. Korbman, J. Reichert, M. Schultze, S. Holzner *et al.*, *Nature (London)* **493**, 70 (2012).
- [15] M. Schultze, E. M. Bothschafter, A. Sommer, S. Holzner, W. Schweinberger, M. Fiess, M. Hofstetter, R. Kienberger, V. Apalkov, V. S. Yakovlev *et al.*, *Nature (London)* **493**, 75 (2012).
- [16] V. Apalkov and M. I. Stockman, *Phys. Rev. B* **86**, 165118 (2012).
- [17] V. Apalkov and M. I. Stockman, *Phys. Rev. B* **88**, 245438 (2013).
- [18] H. K. Kellardeh, V. Apalkov, and M. I. Stockman, *Phys. Rev. B* **91**, 045439 (2015).
- [19] H. K. Kellardeh, V. Apalkov, and M. I. Stockman, *Phys. Rev. B* **92**, 045413 (2015).
- [20] O. Kwon, T. Paasch-Colberg, V. Apalkov, B.-K. Kim, J.-J. Kim, M. I. Stockman, and D. E. Kim, *Sci. Rep.* **6**, 21272 (2016).
- [21] A. K. Geim and K. S. Novoselov, *Nat. Mater.* **6**, 183 (2007).
- [22] A. H. C. Neto, F. Guinea, N. M. R. Peres, K. S. Novoselov, and A. K. Geim, *Rev. Mod. Phys.* **81**, 109 (2009).
- [23] D. S. L. Abergel, V. Apalkov, J. Berashevich, K. Ziegler, and T. Chakraborty, *Adv. Phys.* **59**, 261 (2010).
- [24] H. Aoki and M. Dresselhaus, *Physics of Graphene* (Springer, New York, 2014).
- [25] J. Moore, *Nat. Phys.* **5**, 378 (2009).
- [26] J. E. Moore, *Nature (London)* **464**, 194 (2010).
- [27] X.-L. Qi and S.-C. Zhang, *Phys. Today* **63**(1), 33 (2010).
- [28] D. Hsieh, Y. Xia, D. Qian, L. Wray, F. Meier, J. H. Dil, J. Osterwalder, L. Patthey, A. V. Fedorov, H. Lin *et al.*, *Phys. Rev. Lett.* **103**, 146401 (2009).
- [29] T. Zhang, P. Cheng, X. Chen, J.-F. Jia, X. Ma, K. He, L. Wang, H. Zhang, X. Dai, Z. Fang *et al.*, *Phys. Rev. Lett.* **103**, 266803 (2009).
- [30] Y. Sakamoto, T. Hirahara, H. Miyazaki, S.-i. Kimura, and S. Hasegawa, *Phys. Rev. B* **81**, 165432 (2010).
- [31] J. G. Analytis, J.-H. Chu, Y. Chen, F. Corredor, R. D. McDonald, Z. X. Shen, and I. R. Fisher, *Phys. Rev. B* **81**, 205407 (2010).
- [32] T. Hirahara, Y. Sakamoto, Y. Takeichi, H. Miyazaki, S.-i. Kimura, I. Matsuda, A. Kakizaki, and S. Hasegawa, *Phys. Rev. B* **82**, 155309 (2010).
- [33] A. Kara, H. Enriquez, A. P. Seitsonen, L. C. Lew Yan Voon, S. Vizzini, B. Aufray, and H. Oughaddou, *Surf. Sci. Rep.* **67**, 1 (2012).
- [34] Q. Tang and Z. Zhou, *Progr. Mater. Sci.* **58**, 1244 (2013).
- [35] H. Rostami, A. G. Moghaddam, and R. Asgari, *Phys. Rev. B* **88**, 085440 (2013).
- [36] A. Kormányos, V. Zolyomi, N. D. Drummond, P. Rakytá, G. Burkard, and V. I. Fal'ko, *Phys. Rev. B* **88**, 045416 (2013).
- [37] K. Takeda and K. Shiraiishi, *Phys. Rev. B* **50**, 14916 (1994).
- [38] C.-C. Liu, W. Feng, and Y. Yao, *Phys. Rev. Lett.* **107**, 076802 (2011).
- [39] C.-C. Liu, H. Jiang, and Y. Yao, *Phys. Rev. B* **84**, 195430 (2011).
- [40] Y. Wang, J. Zheng, Z. Ni, R. Fei, Q. Liu, R. Quhe, C. Xu, J. Zhou, Z. Gao, and J. Lu, *Nano* **07**, 1250037 (2012).
- [41] F.-b. Zheng and C.-w. Zhang, *Nanoscale Res. Lett.* **7**, 422 (2012).
- [42] L. Fu, *Phys. Rev. Lett.* **106**, 106802 (2011).
- [43] M. Breusing, S. Kuehn, T. Winzer, E. Malić, F. Milde, N. Severin, J. P. Rabe, C. Ropers, A. Knorr, and T. Elsaesser, *Phys. Rev. B* **83**, 153410 (2011).
- [44] K. J. Tielrooij, J. C. W. Song, S. A. Jensen, A. Centeno, A. Pesquera, A. Z. Elorza, M. Bonn, L. S. Levitov, and F. H. L. Koppens, *Nat. Phys.* **9**, 248 (2013).
- [45] D. Brida, A. Tomadin, C. Manzoni, Y. J. Kim, A. Lombardo, S. Milana, R. R. Nair, K. S. Novoselov, A. C. Ferrari, G. Cerullo *et al.*, *Nat. Commun.* **4**, 1987 (2013).
- [46] I. Gierz, J. C. Petersen, M. Mitrano, C. Cacho, I. C. E. Turcu, E. Springate, A. Stöhr, A. Köhler, U. Starke, and A. Cavalleri, *Nat. Mater.* **12**, 1119 (2013).
- [47] M. W. Graham, S. F. Shi, D. C. Ralph, J. Park, and P. L. McEuen, *Nat. Phys.* **9**, 103 (2013).
- [48] J. C. Johannsen, S. Ulstrup, F. Cilento, A. Crepaldi, M. Zacchigna, C. Cacho, I. C. E. Turcu, E. Springate, F. Fromm, C. Roidel *et al.*, *Phys. Rev. Lett.* **111**, 027403 (2013).
- [49] I. Gierz, F. Calegari, S. Aeschlimann, M. C. Cervantes, C. Cacho, R. T. Chapman, E. Springate, S. Link, U. Starke, C. R. Ast *et al.*, *Phys. Rev. Lett.* **115**, 086803 (2015).
- [50] J. C. Johannsen, S. Ulstrup, A. Crepaldi, F. Cilento, M. Zacchigna, J. A. Miwa, C. Cacho, R. T. Chapman, E. Springate, F. Fromm *et al.*, *Nano Lett.* **15**, 326 (2015).
- [51] F. Bloch, *Z. Phys. A* **52**, 555 (1929).
- [52] W. V. Houston, *Phys. Rev.* **57**, 184 (1940).